11-25-1994

A Prototype Computational Phantom to Create Digital Images for Research and Training in Diagnostic Radiology

Charles F. Babbs
Purdue University, babbs@purdue.edu

A Prototype Computational Phantom to Create Digital Images for Research and Training in Diagnostic Radiology

Charles F. Babbs, David M. Chelberg, Jean Hsu, and Edward J. Delp

Biomedical Engineering Center and School of Electrical Engineering,
Purdue University West Lafayette, IN 47907, USA

November 25, 1994

Abstract-- Research in the processing, compression, transmission, and interpretation of digital radiographic images require the testing and evaluation of a wide variety of images, varying both in format and in spatial resolution. If receiver operating characteristic (ROC) analysis or a related method is used to evaluate the performance of observers using novel vs. conventional displays, large numbers of test images containing known abnormalities are required. This report describes a convenient, inexpensive, and reproducible source of test images, having any desired resolution and containing precisely defined abnormalities of unlimited subtlety. The images are generated by computing x-ray transmission through mathematically defined, three dimensional masses according to Beer's Law. A procedure is presented for generating computer simulated chest radiographs and mammograms, which can contain various classes of abnormalities, including tumors, infiltrates, cavities, pleural effusions, cardiac chamber enlargement, and soft tissue calcifications. Test images can be created from simple computational models of superimposed spherical densities. The approach provides a flexible, inexpensive, easy-to-use research tool for investigators exploring digital techniques in diagnostic radiology. Such simulation software may also be of benefit as a training tool, when employed to generate numerous test images containing subtle abnormalities for programmed instruction and testing.

Key words: computer simulation models, imaging, ROC, training

Supported in pmt by Grant CA-62234 from the National Cancer Institute, Bethesda, Maryland, USA.

I. INTRODUCTION

This report is dedicated to the proposition that computer simulation of x-ray images can be a valuable tool for research and training in radiology. Technology for digital image acquisition, processing, and storage is rapidly becoming available [1] and has the potential in the near future to supplant conventional film-based processes for radiologic image capture, display, and archiving in routine clinical practice. The resolution of digital radiography is fast approaching acceptable limits for many applications [2-5], and digital radiologic workstations [6] are being used clinically. The trend toward digital imaging technology is supported by the increasing computer literacy of radiologists, the development of reasonably priced, high resolution video display terminals, and the rapid evolution of digital image capture technology, including charge coupled devices (CCD's) [4], able to acquire high resolution radiographic images (at least 2000 x 2000 pixels, or about 0.1 mm × 0.1 mm pixel size). As such technology is further developed for general clinical use, there will be a need for a wide variety of test images, containing precisely known normal structures and precisely defined abnormalities.

Of particular importance in the validation of new diagnostic imaging methods is the assessment of system sensitivity and specificity, where the "system" in question includes both a trained radiologist and the imaging technology under evaluation. The most definitive approach to this key issue is receiver operating characteristic (ROC) analysis [7-9], in which curves are generated describing the hit rate for detection of a particular abnormality as a function of the false alarm rate. This type of analysis has become accepted as the most rigorous and objective means of comparing diagnostic imaging methods in radiology in terms of their sensitivity and specificity [7, 8]. To compare the performance of observers using a modified or innovative imaging system with the performance of the same observers using conventional technology, it is necessary to gather performance data for a series of test images, numbering approximately 100, in which the true abnormal vs. normal state is known [8, 9]. In the case of clinical material diagnostic truth can be determined post hoc by biopsy, subsequent clinical course, etc. [10] Another approach is to establish truth by consensus opinion of board ce1tified radiologists [11]. Both approaches are relatively costly, tedious, and productive of limited numbers of test images within a given diagnostic class.

The use of computer models emulating the physics of x-ray absorption by three dimensional tissue masses, positioned in a geometric workspace between a radiation source and a detector array, can provide a useful source of physically realistic test images. The potential advantages of computer generated images, rather than actual clinical radiographs, are that

(1) the true normal/abnormal state of the images is known exactly, since the abnormalities are deliberately created and mathematically defined;

(2) the number of possible abnormalities is unlimited, and the nature, background, and context of the abnormalities can be systematically varied to determine under what circumstances perception and diagnostic performance are most and least influenced by particular digital display techniques;

(3) the marginal cost of obtaining images for analysis (at any desired resolution prior to display) is minimal;

(4) for many psychophysical experiments the entire radiographic process can be simulated automatically at a computer-based workstation for efficient, objective data collection and analysis; and

(5) the fundamental questions regarding the virtue of various digital radiographic techniques as aids to human perception and diagnostic performance can be answered without exposing human subjects to additional radiation.

Accordingly, we have created a general purpose C-language program library to implement such computational phantoms for chest radiography and for mammography.

II. METHODS

Model Space

The general approach to computer simulation of radiographic images is shown in Figure 1. Transmission images are computed using a straightforward line-integration algorithm for x-rays arising from a defined point source, passing through a simulated tissue volume, and striking an image plane, where a phosphor/film surface, charge coupled device (CCD), or other radiologic detector would be located. The relative number of photons reaching any point in the image plane is computed using Beer's Law for absorption of photons by radiodense materials [12, 13].

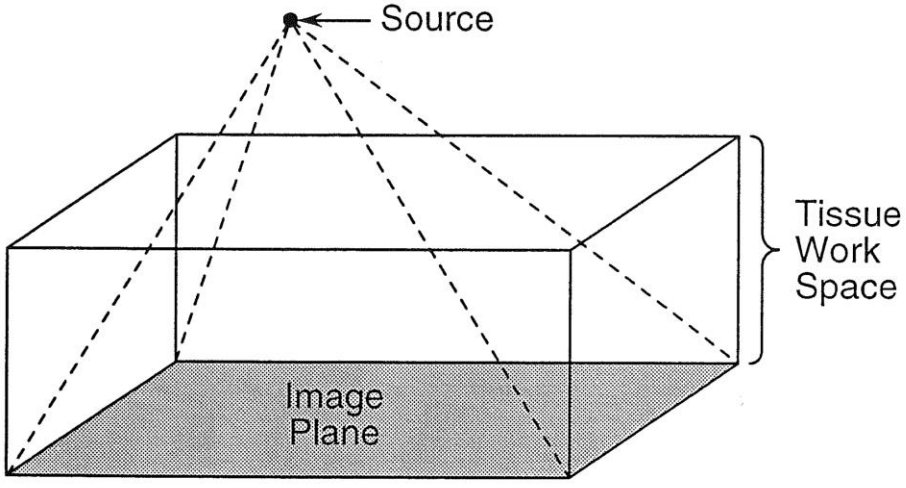

Fig. 1. Scheme for computer simulation of tissue x-ray absorption. The x-ray source may be located at any desired distance from the target tissue.

Inputs to the C-language program implementing the algorithm are read from a control file that specifies the dimensions of the workspace and coordinates of the source. A window on the image plane borders one side of the workspace and is divided to the desired spatial resolution using a rectangular grid, the coordinates of which correspond to picture elements (pixels). Objects in the scene consist of sets of overlapping spheres of varying size, density, and position, as specified by the user in a table read from a control file. With a little practice, the size, density, and three dimensional coordinates of the larger spherical primitives for all computational phantoms were readily specified by one of us (CFB), having knowledge of human anatomy and pathology. Parameters specifying clusters of smaller, randomly oriented spheres in some models were generated by a utility program, and included in the control file for a particular computational phantom. The choice of simple spherical primitives was made to establish proof of concept, and resulted in surprisingly realistic images, which can be further enhanced in future work using more complex geometric shapes.

Computational Approach

To perform the actual line integration describing x-ray transmission through each phantom, the tissue space is divided into n_z equal slices parallel to the image plane. The radiation transmission from the source, through each tissue slice at successive z levels, beginning closest to the source and ending at each indexed pixel, is computed using the expression: $dI(z) = -I(z)\mu dL$, where $dI(z)$ is the amount of attenuation in the number of transmitted photons passing through level, z ; $I(z)$ is the incident radiation intensity at level, z ; μ is the linear attenuation coefficient for monochromatic radiation; and dL is the length of the ray segment in slice dz , computed as the product of dz and the cosecant of angle from source to indexed pixel in the image plane [12]. Linear attenuation coefficients of the target masses are initially read from the control file, which also specifies the diameter and center coordinates of each spherical mass. For economy of language in the following discussion, the term "density" is often used as a synonym for "linear attenuation coefficient" in describing the properties of tissue models.

The general structure of the simulation program is as follows:

```
read tissue dimensions and source coordinates from control file
read water density and added mass densities from control file
for (each z-level slice of the tissue model from incident surface to image plane) {

        include tissue densities in array D(x,y) using subroutine "addmasses"
        for (each pixel x,y in image plane, I(x,y)) {
                find address x' ,y' where incident rays intersect indexed z-level,
                compute the local attenuation in transmitted radiation at x' ,y',
                and store current percent transmission in I(x,y) -- this
                is the incident radiation for next z-level
        }
}
change final percent transmission to percent absorption = "image" values
write suitably scaled image I(x,y)
```

Simulation of Film Processing

The image stored in plane I(x,y) can be thought of as the analog of the latent image captured in exposed, undeveloped film, or even more straightforwardly, the set of values captured by an array of charge coupled devices. In practice, radiographic technique (kVp and mAs), choice of film, and conditions of development are adjusted through trial-and-error to create a visible image, in which clinically relevant information is centered in a gray scale ranging from nearly black to nearly white. In using computational phantoms, this process is simulated by simple linear transformation of raw image values, or "histogram stretching" [14], such that the gray scale values of interest in the image are distributed over the black-to-white range of the final display device, such as a printer or video screen. For example, if the printer can display 256 gray levels, specified by integer values, then the double precision floating point values in I(x,y) are scaled and stretched to span the range 0 to 255, and the test image is written and stored in 8-bit binary words. (The roughly linear relationships between x-ray film exposure and the optical density of the developed radiograph, and in turn between optical density and the physiologic response of the eye to light have been discussed by Meredith and Massey. [15]) Using such linear scaling, one may readily obtain images that are similar in contrast to clinical radiographs.

Addition of Spherical Masses

Before computation of the radiation attenuation in each tissue slice, a density array corresponding to each tissue plane at level, z, parallel to the image plane, is initialized to zero. Then the stored array of input spherical masses is tested to identify masses intersecting the test plane at level z. When such a mass is found, the region in the indexed tissue slice near its center is scanned by a "flying spot", and at each scanned node the inequality

$$(x - x_0)^2 + (y - y_0)^2 + (z - z_0)^2 \leq r^2$$

for the spherical mass of radius, r, centered at x_0 ,y_0, z_0 is evaluated to define the circular section present within the slice at that level, and the corresponding nonzero values for the linear attenuation coefficients are set. Later density values that are added to the test plane overwrite earlier density values, rather than summing with them. As will be seen, this feature provides a convenient means of modeling complex three dimensional objects using simple spherical primitives.

Ray Indexing

After all masses are incorporated in the indexed tissue slice, then, for each pixel in the image plane, a ray is drawn from the x-ray source through the slice to the center of the pixel. The points of intersection of the straight rays with the indexed tissue plane are then computed, and the attenuation, dI, of each indexed ray is computed using Beer's Law. The attenuated intensity, I, of the emerging ray, which is equal to the incident intensity for the next tissue plane, is stored for each pixel. This process is repeated for successive tissue slices between the source and the

image plane. In this way x-ray transmission through the sample is computed by working with one z-level at a time, therefore requiting only one two dimensional array, D(x,y), for storing density information and one two dimensional array, I(x,y) , for storing the transmitted image. The density array is erased and re-written for each successive z-level of the integration, so that the complete three dimensional tissue density array need not be stored in memory all at once.

III. RESULTS

Validation

The C-language code for creating two-dimensional transmission images was validated by analysis of the size and position of shadows cast by standard test spheres placed at various known locations and irradiated from various perspectives. Computed results were compared to those expected from geometric calculations, with good agreement within the limits of resolution tested.

Normal Chest Models

Figure 2 shows a computed digital image in the postero-anterior projection of a chest phantom having homogeneous lung fields of uniform density. In this and subsequent figures "positive" radiographic images are presented, in which areas of high x-ray absorption are rendered black and areas of high x-ray transmission are rendered white. This format is more compatible with laser printed output and duplication in journals. The phantom imaged in Fig. 2 was created by superposition of 82 overlapping spherical masses, as listed in Table 1. For this stylized and minimally complex model the additional lung densities identified as "Random Pulmonary Set 1" and "Random Pulmonary Set 2" were omitted. The dimensions of the model are 40 cm width, 40 cm height, and 20 cm antero-posterior depth. The outer bony shell is truncated anteriorly and posteriorly by the relatively narrow depth of the work space, such that bony elements, except for the added spine and sternum, are not represented in the central portions of the image.

Fig. 2. Computed digital image in the postero-anterior projection of a chest phantom having homogeneous lung fields of uniform density. The model includes 82 spherical masses, included in whole or in part within a 40 x 40 x 20 cm volume. Literature values assumed for linear attenuation coefficients of 60 keV photons [27] are 0.21 cm^{-1} for soft tissue, 0.63 cm^{-1} for bone, and 0.008 to 0.02 cm^{-1} for ventilated lung parenchyma. The image resolution is 500 x 500 pixels. The original image was printed on a Linotype Model L-300 Imagesetter (with RIP 4) having a dot density of 2540 dots per inch from a PostScript file derived from an original 8-bit image of 256 gray levels per pixel. The gray scale is inverted compared to that in a film based radiograph.

TABLE I
Typical Component Elements of a Chest Phantom

Mass Diameter (cm)	Extinction coefficient (scaled units*)	Center x coordinate (cm)#	Center y coordinate (cm)#	Center z coordinate (cm)#	Anatomic identity
20	50	10	10	10	Right shoulder tissue
20	50	30	10	10	Left shoulder tissue
40	100	20	18	10	Chest wall upper
40	100	20	29	10	Chest wall middle
40	100	20	40	10	Chest wall lower
39	2	20	18	10	Lungs upper periphery
39	2	20	29	10	Lungs middle periphery
39	2	20	40	10	Lungs lower
25	3	20	18	10	Lungs upper core
25	5	20	29	10	Lungs middle core
**	**	**	**	**	Random Pulmonary Set #1
**	**	**	**	**	Random Pulmonary Set #2
35.0	50	15	47.1	012	Right hemidiaphragm
35.0	50	25	48.1	012	Left hemidiaphragm
6.0	0	28	35.5	15	Gastric gas bubble
7.0	50	20.0	05	8	Mediastinum
7.0	50	20.0	10	8	
8.0	50	20.5	15	8	Aortic knob
9.0	50	20.5	20	8	Pulmonary veins
7.0	50	20.5	25	8	
6.0	150	20	3	4.7	Bamboo spine
6.0	150	20	6	4.2	
6.0	150	20	9	3.8	
6.0	150	20	12	3.5	
6.0	150	20	15	3.3	
6.0	150	20	18	3.2	
6.0	150	20	21	3.1	
6.0	150	20	24	3.1	
6.0	150	20	27	3.2	
6.0	150	20	30	3.3	
6.0	150	20	33	3.4	
6.0	150	20	35	4.5	
6.0	150	20	38	4.6	

(TABLE I continued)

11.10	50	25.1	27.6	13.9	Left ventricle
8.10	50	22.1	26.6	14.9	Right ventricle
7.10	50	23.1	22.6	11.9	Left atrium
9.10	50	20.0	26.1	12.9	Right atrium
2.60	50	17.0	30.0	10.8	Inferior vena cava
2.60	50	17.0	31.0	10.8	
2.60	50	17.0	32.0	10.8	
2.60	50	17.0	33.0	10.8	
6.66	150	20.0	10.33	22.0	Sternum
6.66	150	20.0	12.33	22.0	
6.66	150	20.0	14.33	22.0	
6.66	150	20.0	16.33	22.0	
6.66	150	20.0	18.33	22.0	
6.66	150	20.0	20.33	22.0	
6.66	150	20.0	22.33	22.0	
6.66	150	20.0	24.33	22.0	
6.66	150	20.0	26.33	22.0	
2.00	52	17.00	18.00	10.0	Right main PA
2.00	52	16.00	18.00	10.0	
2.00	52	15.00	18.00	10.0	
2.00	52	14.00	18.00	10.0	
1.60	52	14.00	17.00	10.0	Right PA apical branch
1.50	52	13.70	16.00	10.0	
1.40	52	13.30	15.00	10.0	
1.30	52	13.00	14.00	10.0	
1.60	52	13.50	18.00	10.5	Right PA middle lobe branch
1.50	52	12.50	18.50	12.0	
1.40	52	11.50	19.00	12.5	
1.30	52	10.50	19.50	13.0	
1.60	52	13.70	18.00	10.0	Right lower lobe branch
1.50	52	13.30	19.00	09.0	
1.40	52	13.00	20.00	08.0	
1.30	52	12.70	21.00	07.0	
2.00	52	23.00	17.00	10.0	Left main PA
2.00	52	24.00	17.00	10.0	
2.00	52	25.00	17.00	10.0	
2.00	52	26.00	17.00	10.0	
1.60	52	26.00	16.00	10.0	Left PA apical branch
1.50	52	26.30	15.00	10.0	
1.40	52	26.70	14.00	10.0	
1.30	52	27.00	13.00	10.0	

(TABLE I continued)

1.60	52	26.50	16.00	10.5	Left lower middle lobe branch
1.50	52	27.00	15.80	12.0	
1.40	52	27.50	15.60	12.5	
1.30	52	28.00	15.40	13.0	
1.60	52	26.30	18.00	10.0	Left lower lobe branch
1.50	52	26.70	19.00	09.0	
1.40	52	27.00	20.00	08.0	
1.30	52	27.30	21.00	07.0	
8.25	150	20.00	5.7	21.3	Manubrium
224.00	0	20.00	-40.0	120.0	Anterior clear area

* Linear extinction coefficient values in the control file are scaled to integer values ranging from 0 to 255 (8-bits) for economy of data storage in memory. Here the linear extinction coefficient for water (0.214 cm^{-1} is scaled to the integer value 50; in these units the maximal possible extinction coefficient is 255 (1.091 cm^{-1}). Prior to actual computation the stored integer values are reconverted to units of cm^{-1} .

Spatial co-ordinates are in cm from the origin, located at the left, inferior, posterior comer of the workspace.

A specific sequence of superposition of masses, indicated in Table 1, was used to create an increasingly complex pattern. Importantly, the order of incorporation of the spherical densities is often critical to the appearance of the final image. In the minimally complex phantom of Figure 2 the soft tissues of the shoulder and the bony structures of the chest wall are defined first. The peripheral bony shell of the "ribs" is created by overwriting the three dense spherical solids of average chest wall density and right-left diameter with slightly smaller, concentric the low density spheres representing peripheral lung tissue. Then water densities of the hemidiaphragms (the right more cranial than the left) and underlying abdominal viscera (with gastric gas bubble) are added. The mediastinum is represented as a vertically telescoped stack of spheres of water density, and the spine as a telescoped stack of spheres of bone density. Next cardiac chambers and great vessels are added. A sternum is added as a chain of tangential slices of bone density spheres centered outside the model space anteriorly. Finally, pulmonary arteries are added as branched series of telescoped spheres of decreasing diameter toward the periphery.

Figures 3(a) and 3(b) show the effect of introducing 2000 additional random elements (pulmonary sets 1 and 2 in Table I) to create detail and texture within the lung fields. In this computational model the upper lung fields, initially assigned density values twice that of the 82-element model shown in Figure 2, were overlaid by a mosaic of 1000 random masses of mean diameter 3 cm and mean density 1/25th that of water. The lower lung fields were similarly overlaid by 1000 random masses of mean diameter 4 cm and mean density 2/25ths that of water. Gaussian variation in both diameter and density of the random pulmonary spheres within specified ranges aided in achieving an organic effect. The mean density for the upper lobes is less than the mean density for the lower lobes to simulate the normal base-to-apex gradient of ventilation/perfusion. (The increased density near the top of Fig 3(b) is "shoulder muscle".)

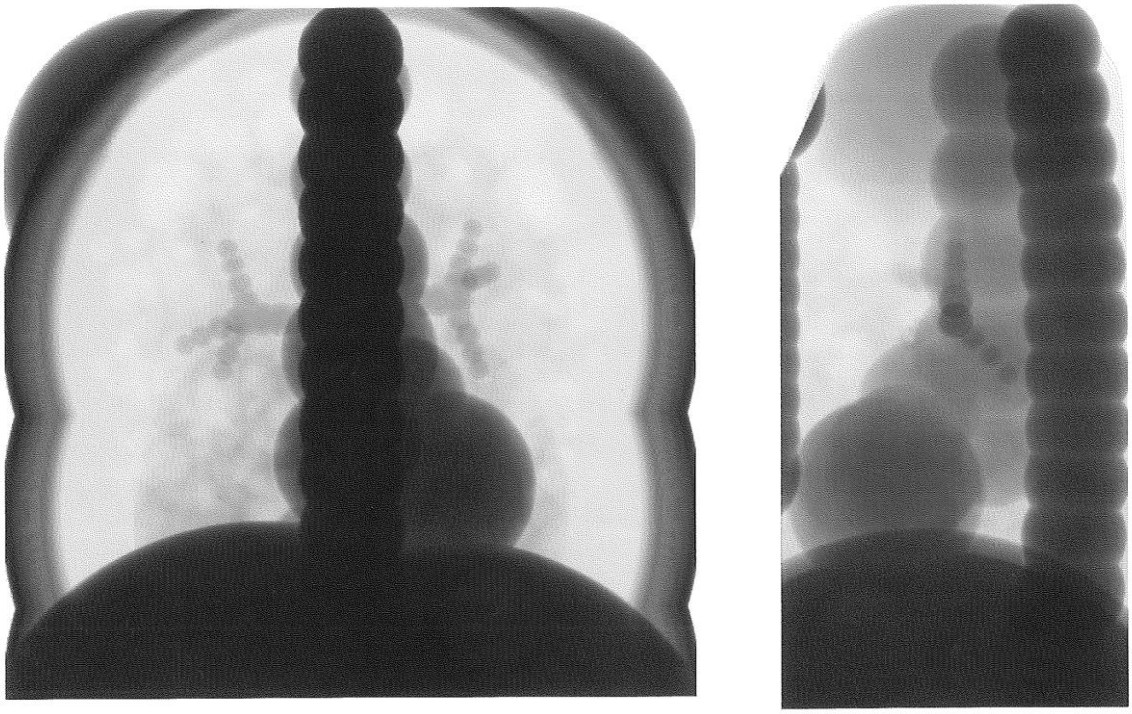

(a) (b)

Fig. 3. Computed digital images of a 2082 element chest phantom having lung field complexity enhanced by addition of 2000 random spherical masses. The 82 large scale anatomic primitives are the same as in Figure 2. The upper light and left lung fields include 1000 non-overlapping random volume densities ranging from 1 to 5 cm in diameter (mean 3 cm) and having a mean linear attenuation coefficient 4% that of soft tissue, comprising 28% of lung volume and embedded in a matrix having linear attenuation coefficient 8% that of water at the periphery and 12% that of water centrally. The lower right and left lung fields include 1000 non-overlapping random volume densities ranging from 1 to 5 cm in diameter (mean 3 cm) comprising 26% of lung volume and having a mean linear attenuation coefficient 8% that of soft tissue and embedded in a matrix having linear attenuation coefficient 12% that of water at the periphery and 20% that of water centrally. (a) postero-anterior projection (b) lateral projection.

Chest Abnormalities

Figures 4 through 7 illustrate a variety of chest abnormalities that can be simulated with computational phantoms. In Figure 4(a) composite model illustrating complications of chronic obstructive pulmonary disease is presented. These include five large apical bullae in the left upper lobe and a left lower lobe infiltrate, recognizable as being posterior from the clear silhouette of the left heart border. There is a right sided pneumothorax; the right hemithorax is hyperexpanded; and the mediastinum is shifted to the left. Here a comparison of a more simple, 91 element model (Fig. 4(a)) with a more complex, 1091 element model (Fig. 4(b)) is presented.

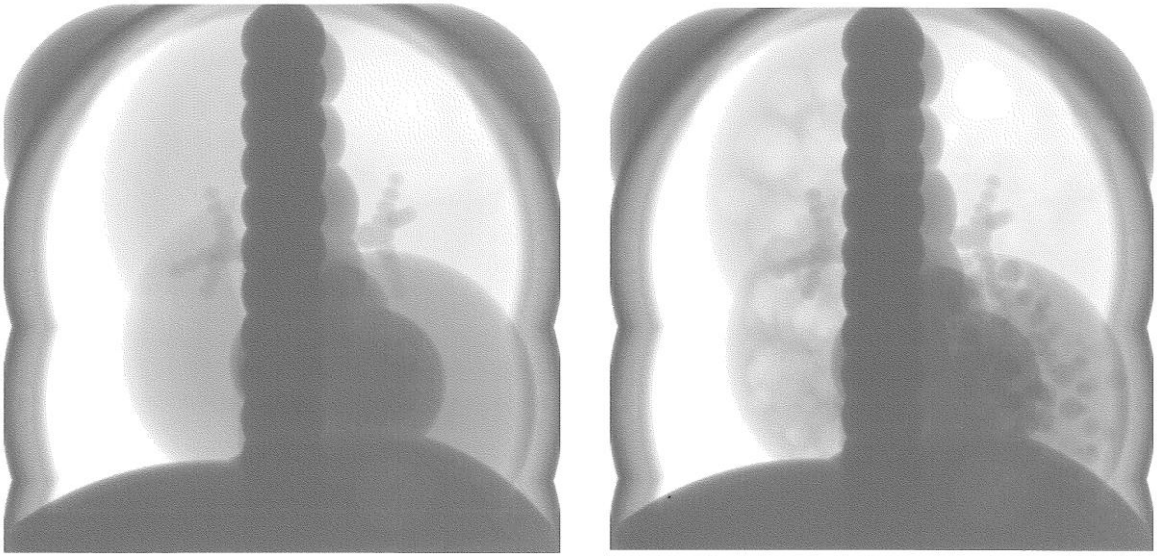

(a) (b)

Fig. 4. Composite simulated chest radiographs demonstrating a variety of possible abnormalities in a hypothetical patient with chronic obstructive pulmonary disease. There is a right sided pneumothorax; the right hemithorax is hyperexpanded, and the mediastinum is shifted to the left. There are 5 large apical bullae in the left upper lobe and a left lower lobe infiltrate, recognizable as posterior in location from the clear silhouette of the left heart border. (a) simple 91 element model with uniform left lower lobe infiltrate. (b) 1091 element model, including in the upper lung fields 500 non-overlapping random spherical volumes, 1 to 5 cm in diameter, having linear attenuation coefficients 2% to 4% that of tissue water (relatively well ventilated or emphasematous lung) embedded in matrix having linear attenuation coefficient 14% that of water, and to create an irregular patchy infiltrate in the left lower lung region using 500 non-overlapping random spherical volumes of water density, 0 to 2 cm in diameter, embedded in matrix having linear attenuation coefficient 40% that of water.

In Fig. 5 several simulated disorders of lung water are illustrated in a hypothetical patient with severe congestive left heart failure. There are bilateral pleural effusions and interstitial pulmonary edema. The effusions were created by placement of spherical water densities in the regions of the costo-phrenic angles. The left atrium and left ventricle are dilated and the right heart chambers are slightly dilated, compared to the normal model.

Fig. 5. Composite simulated postero-anterior chest radiograph demonstrating a variety of abnormalities in a hypothetical patient with severe congestive left heart failure. There is twice normal density in the peripheral and central lung fields, representing interstitial pulmonary edema. There are right and left pleural effusions of water density. Lung fields include 1000 non-overlapping random densities, 1 to 5 cm in diameter, having linear attenuation coefficients averaging 8% that of water, twice that of the normal model. The left atrium and left ventricle are dilated and the right heart chambers are slightly dilated, compared to the normal model.

Fig. 6(a) is an image of a computational phantom representing a hypothetical patient with multiple complications of occupational lung disease. The composite collection of abnormalities includes a spiculated primary carcinoma in the right upper lobe, laterally, right hilar·adenopathy representing metastasis to regional lymph nodes, calcified granulomas of histoplasmosis, diffuse interstitial fibrosis, and a patchy left lower lobe infiltrate. The primary cancer in the mid-right upper lobe (peripheral and less dense than the calcified nodules) was simulated as an irregular, peripheral stellate mass, created by application of the erosion principle, sketched in Fig. 6(b). The tumor density remaining after overwriting a soft tissue density sphere with partially overlapping lung density spheres of various sizes has numerous concavities as well as convexities, separated by sharp ridges and spicules. To create the left lower lobe infiltrate, the background lung density was overwritten with a random cluster of 200 half-water-density spheres, representing partially flooded lung lobules.

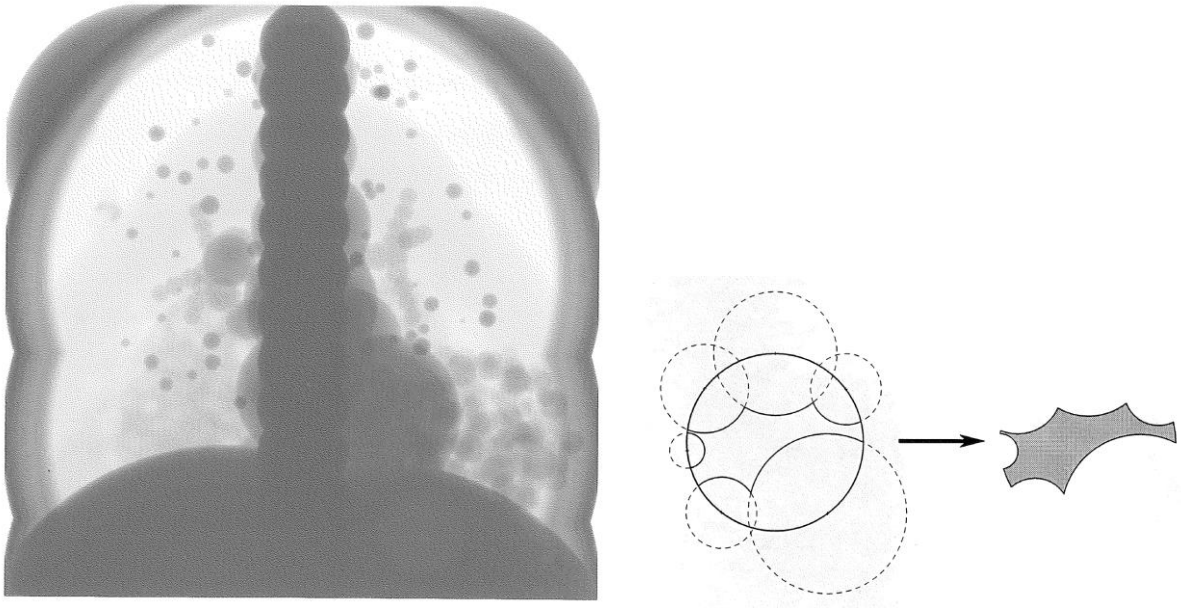

(a) (b)

Fig. 6. (a) Composite simulated chest radiograph demonstrating a variety of abnormalities in a hypothetical patient with occupational lung disease: a spiculated primary carcinoma in the right upper lobe, laterally, right hilar adenopathy, calcified granulomas of histoplasmosis, diffuse interstitial fibrosis, and a patchy left lower lobe infiltrate. This computational phantom includes 1401 spherical densities. Calcified granulomas are simulated by a random cluster of 100 non-overlapping spheres of bone density and average diameter 0.5 cm (range 0.2 to 2 cm). Hilar lymph nodes are simulated by a random cluster of 10 partially overlapping spheres of water density and average diameter 2 cm (range 1 to 4 cm). The patchy left lower lobe infiltrate is simulated by a random cluster of 200 non overlapping spheres of half water density averaging 1 cm in diameter ± 1 cm S.D. Other anatomic features are as in Figure 2. (b) Erosion concept for creation of complex solids by superposition of spherical primitives. An initial solid density is overlaid with surrounding spheres of background density, which partially replace the original.

Figure 7 illustrates a computational phantom that mimics a patient with disseminated cancer. Pulmonary metastases of various sizes were generated as a single random cluster. The patchy right lower lobe pneumonia includes 200 random densities 10% that of water, averaging 5 ± 1 cm in diameter embedded in a matrix having 80% of normal soft tissue density, and replacing 39 percent of the matrix volume locally. The left upper lobe exhibits a wedge-shaped density simulating a pulmonary infarction, which was created by erosion of a single 8 cm diameter peripherally located sphere of two-thirds water density with three more centrally located spheres of ordinary lung density. Together, the composite images in Figures 4 through 7 illustrate the variety of abnormalities can be simulated by computational phantoms comprised solely of tessellations or mosaics of radiodense spheres.

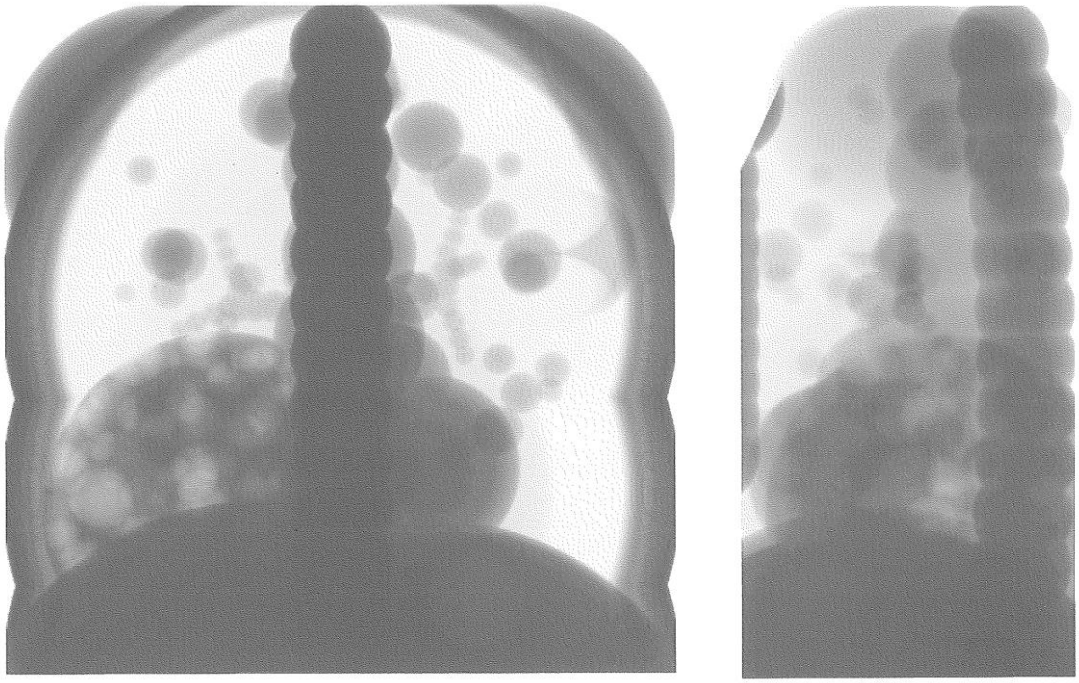

(a) (b)

Fig. 7. Image of a computational phantom simulating findings in a patient with disseminated carcinomatosis: right lower lobe pneumonia, multiple pulmonary metastases, and wedge shaped left upper lobe pulmonary infarction. This simple phantom includes only 337 primitives without added lung field detail. The patchy right lower lobe pneumonia includes 200 random densities 10% that of water, averaging 5 ± 1 cm in diameter embedded in a matrix having 80% of normal soft tissue density, and replacing 39 percent of the matrix volume locally. Note silhouette sign at right heart border. The wedge shaped pulmonary infarct was created with 4 spherical objects centered at the apices of a tetrahedron: a spherical core tangent to the chest wall superimposed with three normal lung density spheres, located medially, antero-medially, and postero-medially. The tumor metastases are a random cluster of 50 water density masses with diameter 3 ± 1 cm (range 1 to 5 cm). (a) Postero-anterior projection. (b) Lateral projection. Note lower lobe infiltrate obscuring retrocardiac clear area. Left ventricular silhouette against background of the lower lobe infiltrate in the lateral projection confirms its right sided, rather than left sided, location.

Mammograms

Breast models are also easily created computationally from simple spherical primitives. First two large, concentric hemispheres, the outermost of non-fat (skin) density and the innermost of fat density, are defined. These large hemispheres are doubly truncated at the north and south poles by the limited dimensions of the work space, leaving the middle third, to simulate breast tissue that is flattened between compression plates during mammographic examination. Within this matrix a Swiss-cheese-like reticulum of nonfat tissue can be created by overwriting an inner non-fat tissue core with random populations of smaller, partially overlapping spheres of fat density. The non-fat tissue core is created as a random cluster of partially overlapping water density spheres, extending to within one cm of the skin surface, where fat density subcutaneous tissue is located. This inner non-fat density core is overlaid and largely replaced with a second random cluster of fat density spheres. The result is an arrangement of non-fat and fat density tissue in which simulated fat lobules of the breast are surrounded by non-fat density glandular and connective tissue in a reticular pattern. If desired, branched chains of smaller spherical densities may be added to mimic lactiferous ducts. In a final optional step, spherical or multi-nodular· tumors may be incorporated, with or without small clusters of microcalcifications--all by the geometric superposition of spherical masses of the desired size.

Figure 8(a) illustrates a computer simulated mammogram derived from a mathematical, computer model containing a breast-like hemisphere 8 cm in radius and "compressed" by truncation to 6 cm thickness in the cranio-caudal dimension. The x-ray source was located 60 cm above the caudal edge of the breast model, at which was located the image plane. The raw transmission image was subjected to a linear histogram stretch to achieve contrast similar to that in clinical mammograms. A carcinoma-like mass with associated microcalcifications is illustrated in the very center of the image. The stellate mass was created by erosion of a spherical density by multiple peripheral spheres of background density, as shown in Fig. 6(b). This arrangement was subsequently overlaid by random cluster microcalcifications of high density. Here, with gray scale reversal, more radiodense areas appear dark, and less radiodense areas appear light.

In Figure 8(b) the same computational model is shown as it would appear medio-lateral compression. To simulate with dual, 90 degree bi-plane images, similar to those taken in current clinical mammography, the center coordinates of the spherical masses in the cranio-caudal model were transformed to simulate compression of a constant-volume soft tissue mass in a plane perpendicular to the original direction of compression.

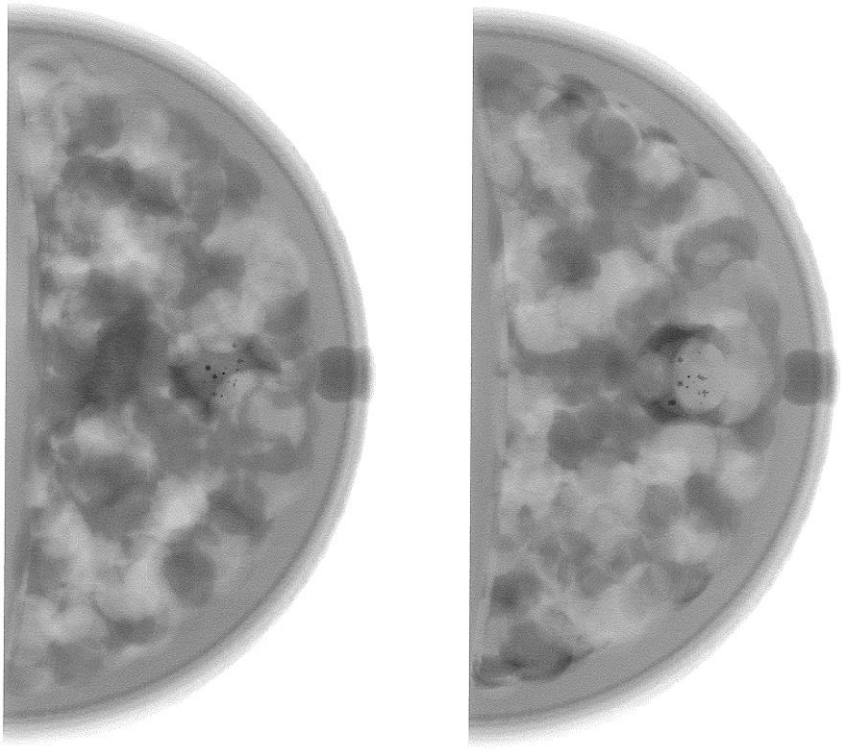

(a) (b)

Fig. 8. Computer simulated mammograms derived from a computational phantom containing a breast-like hemisphere, 8 cm in radius, "compressed" by truncation to 6 cm thickness. Scaled literature values [27] of linear attenuation coefficients for 30 keV photons (as recommended for mammography [28]) in soft tissues of the breast are utilized in the computational phantom: 0.26 cm^{-1} for fat, 0.38 cm^{-1} for non-fat, and 0.39 cm^{-1} for tumor, and 0.36 cm^{-1} for water [27]. The model work space has dimensions (x,y,z) of 8 x 16 x 6 cm, and is irradiated along the z-axis. Concentric hemispheres, centered at (0,8,3), represent non-fat density dermis and subcutaneous fat. The reticulated pattern of non-fat density tissues was created from an inner cluster of 500 random non-fat density spheres of diameter 1.2 ± 0.2 cm, which were permitted to overlap by as much as one radius or 0.6 cm. This inner cluster of non-fat tissue density spheres was confined to a hemisphere 9.5 cm in diameter and was overwritten by a population of otherwise similar fat density spheres, numbering 1000 and confined to a hemisphere 10.5 cm in diameter to create a reticulated non-fat tissue architecture. Subglandular fat, between the chest wall and non-fat breast tissue is modeled by a large, 30 cm radius fat density sphere centered at x = –29.2 cm from the left border of the tissue workspace. This abnormal mammogram includes also a stellate mass of non-fat density in cranial-caudal compression near the center of the image, simulating a carcinoma. The tumor is created by erosion of a single 2 cm diameter tumor density by eight peripheral spheres of background (fat) density, after which a random cluster of 30 microcalcifications, 4 times soft tissue density, are added. (a) Cranial-caudal view (b) Medial-lateral view after transformation as shown in Fig. 9.

To appreciate this transformation, let the x-y plane be defined here as the plane parallel to the chest wall and the z axis be defined as an axis perpendicular to the x-y plane and passing through the nipple (Fig. 9). To mimic the transformation from cranio-caudal to medio-lateral compression, points x,y,z in the cranio-caudally compressed breast must be mapped into points x',y',z' in the media-laterally compressed breast. Here the principles of the transformation are (1) that the amount of compression is the same in both cases and (2) that the relative distance of sphere centers between the z-axis and the skin surface in the x-y plane is maintained after the transformation. If H_1 is the vertical height and $L_1(z)$ is the horizontal length of the cranio-caudally compressed breast at a given level, z , from the chest wall, which is the same in both compression views, then to achieve the same degree of compression medio-laterally, the compressed dimension L_2 must equal H_1 (i.e. $L_2 = H_1$ = same compressed distance, D, either way). Further, to model isovolumetric internal rearrangement of component masses

$$\frac{x'}{0.5L_2} = \frac{x}{0.5L_1(z)} \quad \text{and} \quad \frac{y'}{0.5H_2(z)} = \frac{y}{0.5H_1} \ ,$$

where $L_1(z) = H_2(z) = 2\sqrt{r^2 - z^2}$, the length of the cord across the breast hemisphere parallel to the chest wall at level z. Using these expressions, and interchanging x' and y' to account for 90 degree rotation of the x-ray beam, the constant volume transformation of the x, y coordinates of sphere centers in the orthogonal view of medio-laterally compressed breast model of radius, r , is simply

$$x' = \frac{2\sqrt{r^2 - z^2}}{D}\, y \quad \text{and} \quad y' = \frac{D}{2\sqrt{r^2 - z^2}}\, x \ ,$$

for all compressed regions in which $2\sqrt{r^2 - z^2} > D$. All other parameters of the simulation are unchanged. For simplicity we assume no distortion of the internal spheres themselves by compression in either dimension, i.e. the internal spherical densities remain spherical in both orthogonal biplane models (Fig. 9). In this manner pairs of simulated orthogonal biplane mammograms can be generated. The effect of the transformation can be appreciated in Figures 8(a) and 8(b). Comparison of the cranio-caudal with the medio-lateral compression views shows rearrangement of soft tissue components, as expected.

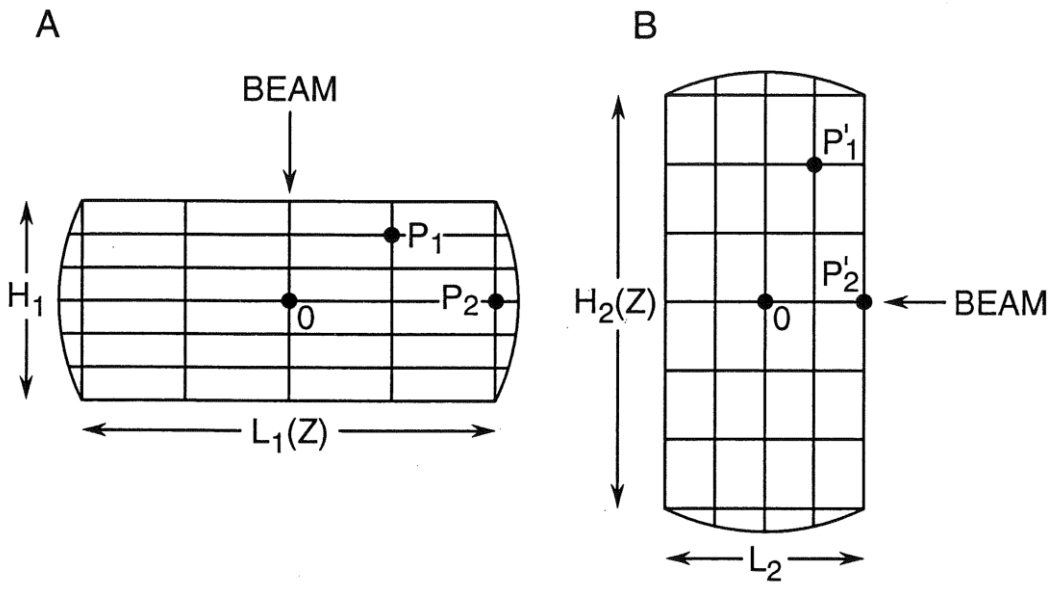

Fig. 9. Scheme for mathematical modeling of an isovolumetric compression of the breast in a plane perpendicular to the initial plane of compression. Sketches represent frontal planes through the compressed breast. Here the drawn plane is parallel to the chest wall, and the z-axis is perpendicular to the plane of the paper. "A" is initial cranio-caudal compression; "B" is the subsequent medio-lateral compression. Tissue volumes initially located at points P_1 and P_2 are translocated to points P_1' and P_2' by medio-lateral compression. In this theoretical transformation the tissue volumes maintain their relative positions with respect to the boundaries of the breast.

IV. DISCUSSION

Using overlapping spherical masses in a computational phantom, it has proved easy to sculpt stylized test images of three dimensional objects that seem sufficiently anatomically realistic for many research applications, including ROC studies [16]. Digital phantoms are inexpensive, safe, flexible, precisely defined, and reproducible. A large number of exactly known abnormalities of varying conspicuity can be included. In principle, digital images of any desired spatial resolution or gray scale resolution can be created. The creation of such models is a form of practical computer art or sculpture, which is seen and interpreted by observers in the form of transmission images, rather than reflection images. Our current software, sample control files, and any future upgrades will be made freely available to colleagues as C-language source code via electronic mail.

In the present project we were surprised to note the degree of complexity and realism achievable with combinations of simple spherical primitives, as anticipated previously by O'Rourke and Badler [17]. The line-integration method also allows shapes other than spheres--such as cylinders and ovoids--to be used. Quite likely, even more realistic models could be created using

combinations of tissue masses defined by ellipsoids or cylinders. These could be added readily by inclusion of subroutines "addellipses" or "addcylinders", similar in action to "addmasses", which read the necessary parameters from formatted control files.

One family of applications of such computational phantoms includes their use as research tools, applied to studies of image enhancement techniques [18, 19] (edge detection, histogram stretching, contrast enhancement, etc.); studies of research in image compression and transmission [5, 20]; studies of resolution requirements for video display devices [2,·21-23]; exploration of three dimensional rendering and reconstruction [16, 24,·25]; or ROC studies of observer performance [7, 9].

It is also possible to model and study degradation of images by various forms of noise or by patient motion. In such research applications the use of computational phantoms also permits comparison of test images with actual slices through the three dimensional density map of x-ray absorbers from which the images were generated. Various figures of merit for comparing alternative display methods can be computed on the basis of the correlation of the test images with the actual densities present.

Another family of possible applications for such computational phantoms includes their use in the training of radiologists--according to a "flight simulator" paradigm, in which artificially generated images with known abnormalities are interpreted by students, either during practice sessions or during testing. Such images could be displayed on video terminals, or copied on conventional film. A classical advantage of computer aided instruction as a supplement to traditional methods of instruction is that training modes can be made interactive, such that the presented images and their degree of difficulty are selected according to the trainee's correct or incorrect responses.

When properly implemented, such branching algorithms for computer aided instruction, which pose problems and respond according to the students' previous decisions, maximize learning rate and minimize boredom, allowing each trainee to be optimally challenged [26]. Depending on the computational speed and storage media available, test images could be either generated on-line or selected from a pre-existing library. Additional features of computer assisted radiological training could readily include incorporation of hints, by which learners are assisted in difficult cases, incorporation of help, wherein certain general rules are reviewed, the ability to zoom the generated image to focus on finer detail in a targeted region, and automatic record keeping and collection of performance statistics. Although early versions of computational phantoms for use in computer aided instruction would be developed by teams including both board certified radiologists and competent computer programmers; advanced versions could be supported by "authoring programs" [26] that allow the non-programming instructor to set up a variety of lessons, incorporating desired normal and abnormal anatomical features. Accordingly, we envision widespread future application of computational phantoms in academic radiology, both for research and for training.

REFERENCES

1. JL Coatrieux, C Toumoulin, C Ramos, and L Luo, "Future Trends in 3D Medical Imaging," *IEEE Engineering in Medicine and Biology Magazine,* vol. 9, No.4, pp. 33-39, December 1990.
2. SJ Dwyer, GG Cox, LT Cook, JH McMillan, and AW Templeton, "Experience with high resolution digital gray scale display systems," *SPIE Medical Imaging IV: PACS System Design and Evaluation,* vol. 1234, pp. 132-138, 1990.
3. JD Newell and CA Kelsey, "Digital radiology of the thorax," in *Digital Imaging in Diagnostic Radiology,* ed. JD Newell and CA Kelsey, pp. 21-42, Churchill Livingstone, New York, 1990.
4. TB Hunter and LL Fajardo, "Digital genitominary, gastrointestinal, and breast radiology," in *Digital Imaging in Diagnostic Radiology,* ed. JD Newell and CA Kelsey, pp. 43-70, Churchill Livingstone, New York, 1990.
5. HP Chan, CJ Vybomy, H MacMahon, CE Metz, K Doi, and EA Sickles, "Digital mammography: ROC studies of the effects of pixel size and unsharp mask filtering on detection of subtle microcalcifications," *Investigative Radiology,* vol. 22, pp. 581-589, 1987.
6. DV Beard, RE Johnston, E Pisano, BM Hemminger, and SM Pizer, "Radiology workstation for mammography: preliminary observations, eyetracker studies, and design," *SPIE Medical Imaging V: PACS Design and Evaluation,* vol. 1446, pp. 289-296, 1991.
7. CE Metz, "ROC methodology in radiologic imaging," *Invest Radiol,* vol. 21, pp. 720-733, 1986.
8. CD Metz, "Some practical issues of experimental design and data analysis in radiological ROC studies," *Investigative Radiology,* vol. 24, pp. 234-245, 1989.
9. JA Swets, "ROC analysis applied to the evaluation of medical imaging techniques," *Invest Radiol,* vol. 14, pp. 109-121, 1979.
10. JK Gohagan, EL Spitznagel, M McCrate, and TB Frank, "ROC analysis of mammography and palpation for breast screening," *Investigative Radiology,* vol. 19, pp. 587-592, 1984.
11. LR Goodman, WD Foley, CR Wilson, AA Rimm, and TL Lawson, "Digital and conventional chest images: observer performance with film digital radiography system," *Radiology,* vol. 158, pp. 27-33, 1986.
12. EE Christensen, TS Cuny, and J Nunnally, *An Introduction to the Physics of Diagnostic Radiology,* pp. 52-67, Lea & Febiger, Philadelphia, 1972.
13. JH Hubbell, *Photon Cross Sections, Attenuation Coefficients, and Energy Absorption Coefficients from 10 KeV to 100 GeV. National Bureau of Standards Handbook 29,* August 1969.
14. JA Richards, "Histogram equalization," in *Remote Sensing Digital Image Analysis,* ed. JA Richards, pp. 91-103, Springer-Verlag, Berlin, 1986.
15. WJ Meredith and JB Massey, *Fundamental Physics of Radiology, Second Edition,* pp. 166-181, Williams and Wilkins, Baltimore, 1972.
16. J Hsu, CF Babbs, DM Chelberg, Z Pizlo, and EJ Delp, "A study of the effectiveness of stereo imaging with applications in mammography," *SPIE Human vision, visual*

processing, and digital display (W), vol. 1913, pp. 154-165, 1993.

17. J O'Rourke and N Badler, "Decomposition of three-dimensional objects into spheres," *IEEE Transactions on Pattern Analysis and Machine Intelligence,* vol. PAMI-1, pp. 295- 305, 1979.
18. PH Eichel, EJ Delp, K Koral, and AJ Buda, "A Method for Fully Automatic Definition of Coronary Arterial Edges from Cineangiograms," *IEEE Transactions on Medical Imaging,* vol. MI-7, No.4, pp. 313-320, December 1988.
19. HL Tan, SB Gelfand, and EJ Delp, "A Comparative Cost Function Approach to Edge Detection," *IEEE Transactions on Systems, Man, and Cybernetics,* vol. 19, No.6, pp. 1337-1349, December 1989.
20. JD Newell, "Teleradiology," in *Digital Imaging in Diagnostic Radiology,* ed. JD Newell and CA Kelsey, pp. 71-77, Churchill Livingstone, New York, 1990.
21. H MacMahon, CJ Vyborny, CE Metz, K Doi, V Sabeti, and SL Solomon, "Digital radiography of subtle pulmonary abnormalities: An ROC study of the effect of pixel size on observer performance," *Radiology,* vol. 158, pp. 21-26, 1986.
22. GT Herman, "A Survey of 3D Medical Imaging Technologies," *IEEE Engineering in Medicine and Biology Magazine,* vol. 9, No.4, pp. 15-17, December 1990.
23. J Owczarczyk and B Owczarczyk, "Evaluation of the true 3D display systems for visualizing medical volume data," *The Visual Computer,* vol. 6, pp. 219-226, 1990.
24. H Fuchs, M Levoy, and SM Pizer, "Interactive Visualization of 3D Medical Data," *IEEE Computer,* pp. 46-51, August 1989.
25. C Smets, D Vandetmeulen, P Suetens, and A Oosterlimck, "A knowledge based system for the 3D reconstruction and representation of the cerebral blood vessels from a pair of stereoscopic angiograms," *Proc SPIE Med Image III,* vol. 1092, pp. 130-138, 1989.
26. ZJ Pudlowski, "Developing computer programs for engineering education--important issues," in *Computer Aided Training in Science and Technology,* ed. E Onate and B Suarez, pp. 34-41, Pineridge Press, Barcelona, 1990.
27. FA Duck, *Physical Properties of Tissue--A Comprehensive Reference Book,* pp. 226-245, Academic Press, London, 1990.
28. "Evaluation of radiation exposure from diagnostic radiology examinations: technique exposure guides for the craniocaudal projection in mammography," *DHHS Publication (FDA) 85-8244,* p. 3, 1985.